

## Research Article

# Band Structure Analysis of $\text{La}_{0.7}\text{Sr}_{0.3}\text{MnO}_3$ Perovskite Manganite Using a Synchrotron

**Hong-Sub Lee and Hyung-Ho Park**

*Department of Materials Science and Engineering, Yonsei University, 50 Yonsei-ro, Seodaemun-gu, Seoul 120-749, Republic of Korea*

Correspondence should be addressed to Hyung-Ho Park; [hhpark@yonsei.ac.kr](mailto:hypark@yonsei.ac.kr)

Received 24 March 2015; Accepted 28 April 2015

Academic Editor: Veer P. S. Awana

Copyright © 2015 H.-S. Lee and H.-H. Park. This is an open access article distributed under the Creative Commons Attribution License, which permits unrestricted use, distribution, and reproduction in any medium, provided the original work is properly cited.

Oxide semiconductors and their application in next-generation devices have received a great deal of attention due to their various optical, electric, and magnetic properties. For various applications, an understanding of these properties and their mechanisms is also very important. Various characteristics of these oxides originate from the band structure. In this study, we introduce a band structure analysis technique using a soft X-ray energy source to study a  $\text{La}_{0.7}\text{Sr}_{0.3}\text{MnO}_3$  (LSMO) oxide semiconductor. The band structure is formed by a valence band, conduction band, band gap, work function, and electron affinity. These can be determined from secondary electron cut-off, valence band spectrum, O 1s core electron, and O K-edge measurements using synchrotron radiation. A detailed analysis of the band structure of the LSMO perovskite manganite oxide semiconductor thin film was established using these techniques.

## 1. Introduction

Oxide semiconductors and their potential application in next-generation devices have received a great deal of attention due to their various optical, electric, and magnetic properties [1–6]. An understanding of the origin of these properties is also very important, for which many studies have employed various analytical techniques. Among the present techniques, spectroscopy, which leverages the interaction between a light source and matter, is very useful, and more than 50 types of spectroscopy techniques are being used for this type of analysis [7, 8]. In this study, we introduce a band structure analysis (band mapping) technique using a soft X-ray energy source to study a  $\text{La}_{0.7}\text{Sr}_{0.3}\text{MnO}_3$  (LSMO) oxide semiconductor. The various characteristics of the oxides originated from the band structure, which is illustrated in a simplified schematic band diagram in Figure 1. The figure shows the valence band, conduction band, band gap “ $E_G$ ” (distance from valence band maximum (VBM) to conduction band minimum (CBM)), work function “ $E_{WF}$ ” (distance from Fermi level to vacuum level), and electron affinity “ $E_{EA}$ ” (distance from CBM to vacuum level) [9]. For band mapping, a variable energy source is required to determine the unoccupied states, and

such a source is available using synchrotron radiation. Basically, band mapping can be measured using two types of techniques, namely, photoelectron spectroscopy (PES) for occupied states and X-ray absorption spectroscopy (XAS) for unoccupied states.

The energy and density of occupied states below the Fermi level can be measured based on the photoelectric effect, which can be attributed to the transfer of energy from the light to an electron in the sample according to classical electromagnetic theory. Therefore, when we measure kinetic energy and the number of electrons emitted from the sample, the energy and density of occupied states can be obtained from energy conservation as  $E_{\text{kin}} = h\nu - E_{WF} - E_{\text{Binding}}$ . A typical PES spectrum is a plot of the number of electrons detected versus the binding energy of these electrons. The binding energy of core electrons can be used to directly identify each element that exists in or on the surface of a sample. Further, according to kinetic energy, the photoelectrons have an inelastic mean free path within 10 nm from the top surface, and emitted photoelectrons therefore provide information specific to the sample surface. All of the photoelectrons from deeper regions, which were generated by X-rays penetrating into the top 1–5 micrometers of the material, are recaptured

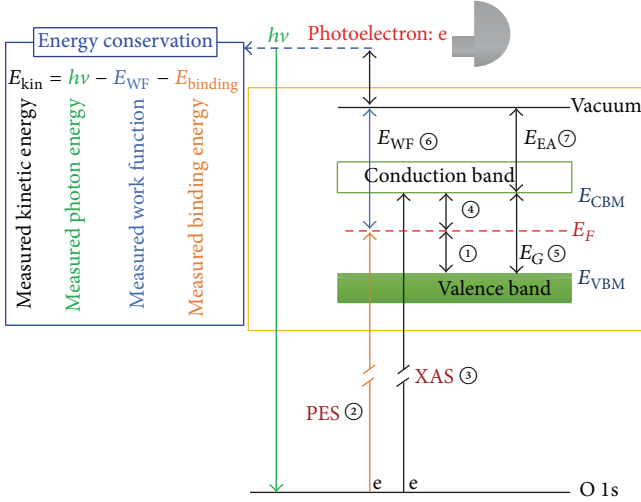


FIGURE 1: Simplified assembly view of the band diagram and measurement principle.

and/or scattered in various excited states within the material. The emitted electrons, which lose energy by scattering, are called secondary electrons and are used to determine  $E_{WF}$ .

XAS measures the excitation of electrons from a core level to partially filled and empty states, as shown in ③ in Figure 1. The core electron of a target atom absorbs an X-ray photon and is elevated from the K (1s) or L (2p) shell to an unoccupied discrete level, thereby creating a core hole. Electrons of higher energy levels fill the hole and release excess energy, either through the radiation of fluorescent photons (bulk-sensitive) or by the emission of Auger electrons (surface-sensitive). XAS spectra are recorded by measuring either the electron yield or fluorescence yield as a function of incident photon energy. Hence, the absorption positions and spectral shape in a NEXAFS spectrum are directly related to the nature of these unoccupied electronic states. Decay in core holes may also occur via the emission of fluorescent photons from the top 200 nm of the film, as opposed to Auger electrons, which are released from the top 10 nm. In this study, electron yield mode was used to measure empty states of a LSMO film. In an oxide semiconductor, when an O 1s core electron is transferred to the unoccupied states of bonded cation atoms via their 2p orbital, the sample absorbs electrons as mentioned above. An O 1s XAS of a LSMO film was obtained to measure the sample absorption current according to energy variation using a pico-ampere meter. Therefore, the O 1s XAS shows both energy and density of unoccupied states. We constructed a band structure using the above values as follows. In an oxide semiconductor, each value in Figure 1, that is, the energy distance ①: from Fermi level to VBM, ②: from O 1s to Fermi level, and ③: from O 1s to CBM, was obtained using a combination of PES and XAS. The energy values were measured from valence band PES (①), O 1s PES (②), and the first derivative of O 1s XAS (③), respectively. Further, the band gap  $E_G$  (⑤) was obtained from ③ - ② = ④ and ① + ④ = ⑤, as shown in Figure 1. In a final step, the work function ⑥ and electron affinity,  $E_{EA}$  ⑦, were defined using a secondary

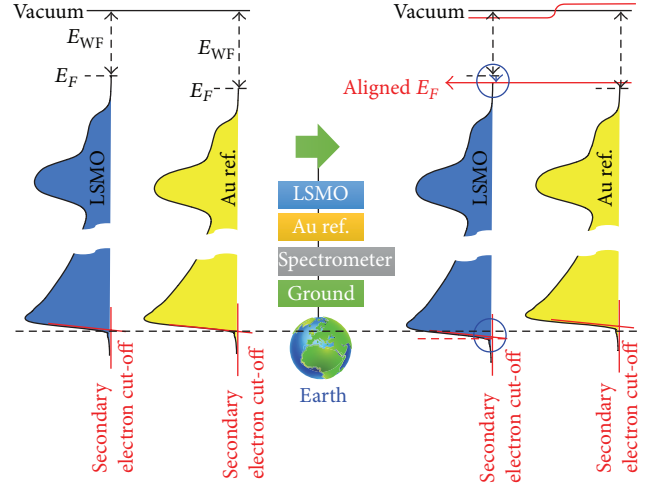


FIGURE 2: A simplified schematic diagram of Fermi alignment in a spectrometer.

cut-off measurement. As shown in Figure 2, when the LSMO film was in contact with sample holder containing reference Au samples, the Fermi levels of all contacted materials were aligned to the spectrometer and/or earth. Therefore, at this state, the measured  $E_{WF}$  value from energy conservation, that is,  $E_{kin} = h\nu - E_{WF} - E_{Binding}$ , corresponded to the work function of the spectrometer. The PES spectrum was shifted by the Fermi alignment, and the shift value was obtained from the secondary cut-off, as shown in the blue circle in Figure 2. The secondary cut-off indicates a zero kinetic energy position of a secondary electron. Therefore, before Fermi alignment, the secondary cut-off of the material was zero. We also measured the shifted secondary cut-off resulting from Fermi alignment, as shown in Figure 2.

The perovskite manganite family, that is,  $R_{1-x}A_xMnO_3$  (where R and A are trivalent rare-earth ions and divalent alkaline-earth ions, resp.), has been of interest due to the colossal magnetoresistance (CMR) and colossal electroresistance (CER) of its members [9–12]. Their magnetic and electric properties can be controlled when the cation site is substituted for different-sized cations or when the composition is changed. The substitution of different sizes of cations and composition variation affect Mn-O bond angle, charge ordering state, and the number of Mn-O bonds [11, 12]. The ideal gross crystal structure of perovskite oxide as a stoichiometry formula of  $ABO_3$  belongs to the cubic space group  $Pm\bar{3}m$  as shown in Figure 3(a), which consists of a three-dimensional framework of corner-shared  $[BO_6]$  octahedron. The A-site cations as trivalent rare-earth and divalent alkaline-earth are located in the dodecahedral sites surrounded by twelve oxygen anions. Although the ideal perovskite structure is centrosymmetric, only a few materials have simple cubic structure at room temperature. This lattice distortion related tendency can be explained by the Goldschmidt tolerance factor ( $t$ ) as follows, in terms of the ionic radii of the atomic species of the structure [13]:

$$t = \frac{R_A + R_O}{\sqrt{2}(R_B + R_O)}. \quad (1)$$

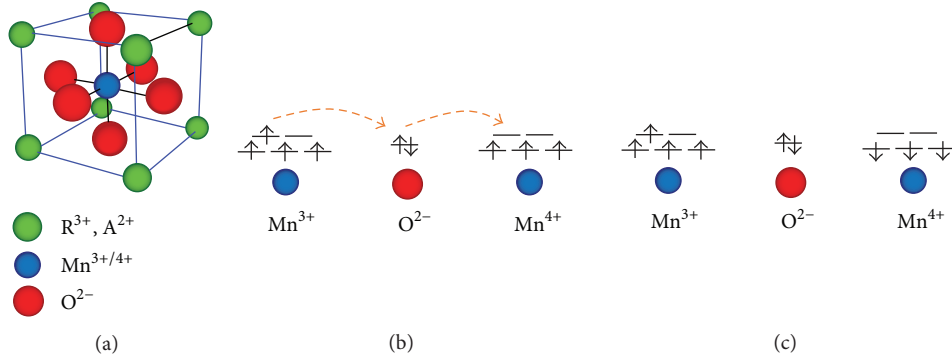


FIGURE 3: Schematic diagrams of (a) ideal cubic structure of perovskite manganite and the double exchange of (b) ferromagnetically and (c) antiferromagnetically aligned Mn-O-Mn chain.

The  $R_A$ ,  $R_B$ , and  $R_O$  denote the ionic radius for the A cation, B cation, and oxygen, respectively. With tolerance factor of 1, the crystal structure of film has ideal cubic structure and this structure has no compressive or tensile internal strain. The perovskite structure is stable for  $0.89 < t < 1.02$ . A variation of  $t$  value from 1 indicates the distorted perovskite structure generation. According to the ionic radius with tolerance factor ( $t$ ), the manganite crystalline state changes to the rhombohedral ( $0.96 < t < 1$ ) and then to the orthorhombic structure ( $t < 0.96$ ), in which the  $\text{Mn}^{3+}\text{-O}^{2-}\text{-Mn}^{4+}$  bond angle is deformed [14].

In the  $R_{1-x}A_x\text{MnO}_3$  material, the filling of the Mn 3d  $e_g^1 \uparrow$  band is controlled by the value of “ $x$ ” in  $R_{1-x}A_x\text{MnO}_3$  with a fully occupied O 2p orbital [15]. Therefore, the state of a fully occupied Mn  $e_g^1$  band,  $R^{3+}\text{Mn}^{3+}\text{O}^{2-}_3$ , is classified as a Mott insulator, and a completely empty Mn  $e_g^1 \uparrow$  band,  $A^{2+}\text{Mn}^{4+}\text{O}^{2-}_3$ , is a band insulator. Both end members are insulators, but the intermediate member is a semiconductor.  $R_{0.7}A_{0.3}\text{MnO}_3$  is classified as a p-type semiconductor or half metal due to its partially occupied Mn  $e_g^1$  band, and the conduction is induced by a double exchange mechanism in the Mn-O-Mn chain [16]. In the double exchange mechanism, the  $e_g$  electron on a  $\text{Mn}^{3+}$  ion can hop to a neighboring site only if there is a vacancy with the same spin direction (since hopping proceeds without spin-flip of the hopping electron) as shown in Figure 3(b). Therefore, the double exchange predicts that this electron movement from one species to another will be facilitated more easily if the electrons do not have to change spin direction in order to conform the Hund rules at the accepting species. Therefore, it is hard for an  $e_g$  electron to hop to a neighboring  $\text{Mn}^{4+}$  ion in which the  $t_{2g}$  spins aligned antiparallel to the  $e_g$  electron spin as shown in Figure 3(c) [16]. Nevertheless, the full understanding of the electronic structure and conduction properties of perovskite manganite remains a challenging problem of strongly correlated system. Therefore, in the present study, we established a spectroscopic method of band structure analysis using a LSMO thin film which is a member of the perovskite manganite family and a well-known CMR and CER material due to its high Neel’s temperature.

## 2. Experimental Details

The films were prepared by RF magnetron sputtering at a thickness of 30 nm on Pt(111)/Ti/SiO<sub>2</sub>/Si(100) substrates. The LSMO powder targets were prepared by a standard solid state reaction method using La<sub>2</sub>O<sub>3</sub>, SrCO<sub>3</sub>, and Mn<sub>2</sub>O<sub>3</sub> powders as starting materials. During the deposition, the working pressure, substrate temperature, and gas flow ratio of Ar : O<sub>2</sub> were maintained as 5 mTorr, 550°C, and 4 : 1, respectively. The phase formation of the films was confirmed by X-ray diffraction. For the band mapping of the LSMO film, the O 1s core electron, valence electron, secondary cut-off, and O 1s K-edge were measured using PES and XAS on the 8A2 beam line of the Pohang Accelerator Laboratory. The O 1s core electron was measured using a source energy of 630 eV. The valence band spectrum and secondary cut-off were obtained at a source energy of 110 eV. Energy calibration was performed using an Au foil at all measurement steps.

## 3. Results and Discussion

**3.1. Valence Band Measurement to Define Fermi Level.** Figure 4 shows valence band spectra of the LSMO thin film and Au reference foil. Normally, a Fermi edge in an oxide semiconductor is not observed, unlike the readily observed Fermi edge of a metal. Therefore, the Fermi edge of the oxide semiconductor must be defined using an Au reference. As shown in Figure 2, the oxide semiconductor material LSMO with an Au reference should be in contact with the holder loaded in the spectrometer. Therefore, the Fermi levels of the materials are aligned to the spectrometer and/or earth. The energy difference from the Fermi level to the VBM in the oxide semiconductor was determined, as shown in the inset of Figure 4. The energy range of the inset in Figure 4 was expanded to the vicinity of the Fermi level, which shows the energy dispersion of the Au Fermi edge based on temperature. At the slightly inclined Fermi edge, the center point was defined as the Fermi level, and the center position was calibrated to zero binding energy. The VBM of the oxide semiconductor was calculated using linear extrapolation of the edge, as in the inset of Figure 4. Therefore, in the LSMO film, the energy difference from the Fermi level to the VBM

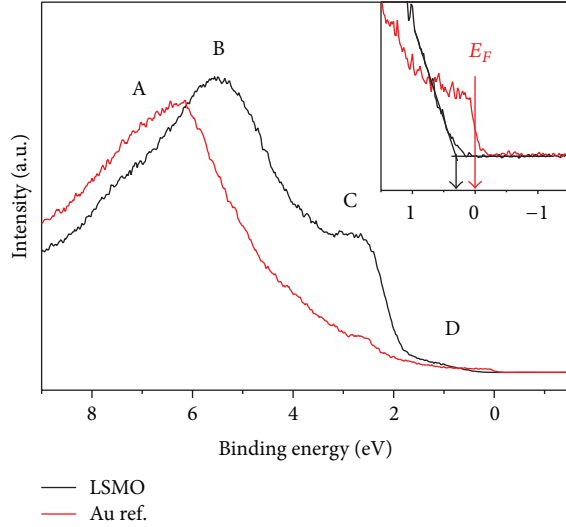


FIGURE 4: Valence band spectra of the LSMO thin film and reference Au. Inset corresponds to expanded data in the vicinity of the Fermi level.

was 0.29 eV. We labeled the band order as A, B, C, and D in the valence band spectrum according to binding energy, as shown in Figure 4. Normally, the band order of LSMO can be identified as A: O 2p-Mn 3d  $t_{2g}$  orbital hybridization state, B: O 2p nonbonding state, C: Mn 3d  $t_{2g}\uparrow$  state, and D: Mn 3d  $e_g^1\uparrow$  state, and these identified band spectra show the electron density of each state [17, 18].

**3.2. Conduction Band Measurement to Define the Conduction Band Minimum.** The conduction band and CBM were measured and defined from the O 1s core electron and O 1s XAS spectrum, and Figures 5(a) and 5(b) show the O 1s core electron and O 1s XAS spectrum of LSMO, respectively. The O 1s PES of LSMO film showed two bonding states for oxygen, labeled as A and B in Figure 5(a), which were identified as surface oxygen and lattice oxygen, respectively [19]. Normally, in perovskite manganite, the surface oxygen is observed in the top surface region, which has a different state from that of the lattice. Figure 5(b) shows O 1s XAS data of the LSMO film and its first derivative of absorption. First, the absorptions in O 1s XAS are labeled as A, B, and C to identify the band according to energy state. From the lowest absorption edge of about 527.5 eV to 533.5 eV (A region), the absorption corresponds to partially empty Mn 3d  $e_g^1\uparrow$ , completely empty  $t_{2g}\downarrow$ ,  $e_g^2\uparrow$ ,  $e_g^1\downarrow$ , and  $e_g^2\downarrow$  bands in energy order. After this Mn 3d absorption region (B region), the absorption from 533 eV to 538 eV corresponds to the transition from O 1s to the completely empty states of A-site cations such as La 5d/4f and Sr 4d. The final absorption region of C shows a transition from O 1s to Mn 4sp [20, 21]. When we subtracted the O 1s binding energy of Figure 5(a) from the O 1s XAS spectrum of Figure 5(b), we obtained a conduction band spectrum starting from the Fermi level, as shown in Figure 5(c). This is because the “binding energy” indicates the energy difference from the Fermi level to the O

1s core level energy. However, it is difficult to correctly define the CBM in O 1s XAS data due to energy dispersion of the O 1s binding energy, that is,  $\Delta E$  (O 1s binding energy):  $\Delta E_{\text{total}} = \sqrt{(\Delta E_{\text{anal.}})^2 + (\Delta E_{\text{photon}})^2 + (\Delta E_{\text{thermal broad}})^2 + (\Delta E_{\text{inhomogen}})^2 + \text{etc.}}$  [22]. Therefore, the CBM level was defined as the maximum value in the first derivative of absorption [23]. As shown in Figure 5(c), the CBM level of the LSMO film was located 0.34 eV from the Fermi level. For O 1s XAS measurement, the energy was calibrated using Au and/or SiO<sub>2</sub>, which have a well-known energy level; in the present study, we calibrated the starting energy using an Au foil. In the case of energy calibration, an induced error in energy change process cannot be calibrated, and this induces an error in the energy difference from the Fermi level to the CBM.

**3.3. Secondary Cut-Off Measurement to Define the Work Function.** As mentioned above, the measured work function value ( $E_{\text{WF}}$ ) in the state was the  $E_{\text{WF}}$  of the spectrometer and/or earth from energy conservation as  $E_{\text{kin}} = h\nu - E_{\text{WF}} - E_{\text{Binding}}$ . Then, from the measurement of the secondary cut-off, we determined the shift value based on Fermi alignment, as shown in Figure 2. If the material had a larger  $E_{\text{WF}}$  value than the spectrometer and/or earth, a secondary cut-off was observed in the vicinity of zero electron kinetic energy. Normally, most materials have a smaller  $E_{\text{WF}}$  value than the spectrometer and/or earth, and the secondary electron cannot reach the hemisphere analyzer due to a kinetic energy value less than zero. Therefore, as shown in Figure 6(a), additional kinetic energy was supplied by an applied negative voltage. In this study, we applied -20 V to the sample holder and we observed the cut-off of a secondary electron of LSMO and the Au ref. Therefore, the secondary cut-off position was defined as the energy shift from a 20 eV kinetic energy. As shown in Figure 6(a), the measured secondary cut-off value of the LSMO film was 19.35 eV, and -0.65 eV was obtained as a shift energy with a 20 eV kinetic energy; therefore, the secondary cut-off was defined by linear extrapolation as VBM. Using the equations  $h\nu - E_{\text{WF}} = E_{\text{F}} - (\text{shift in secondary cut-off})$ , the  $E_{\text{WF}}$  value of LSMO film was measured to be about 4.8 eV, that is,  $110 \text{ eV} - E_{\text{WF}} = 104.55 \text{ eV} - (-0.65 \text{ eV})$  [24].

**3.4. Interpretation of the Electronic Band Structure of LSMO Thin Film.** In the final step, we constructed a band structure using the values measured above. As previously described, the band gap,  $E_{\text{G}}$ , was obtained from  $\textcircled{3} - \textcircled{2} = \textcircled{4}$  and  $\textcircled{1} + \textcircled{4} = \textcircled{5}$ , as shown in Figure 1. The electron affinity,  $E_{\text{EA}}$  ( $\textcircled{7}$ ), was obtained from  $\textcircled{6} - \textcircled{4}$ . The band diagram of LSMO film constructed using these methods is illustrated in Figure 7. The complete band structure offers useful information to help understand the properties, and the interface characteristics can be determined for device applications. For accurate band structure analysis, very accurate energy calibration is required using well-known materials such as Au and SiO<sub>2</sub>. Further, a comparative study at various conditions will provide more meaningful data. For example, we measured the valence band PES, O 1s PES, and O 1s XAS of (La<sub>0.7</sub>)Sr<sub>0.3</sub>MnO<sub>3</sub>, (La<sub>0.6</sub>Gd<sub>0.1</sub>)Sr<sub>0.3</sub>MnO<sub>3</sub>, and

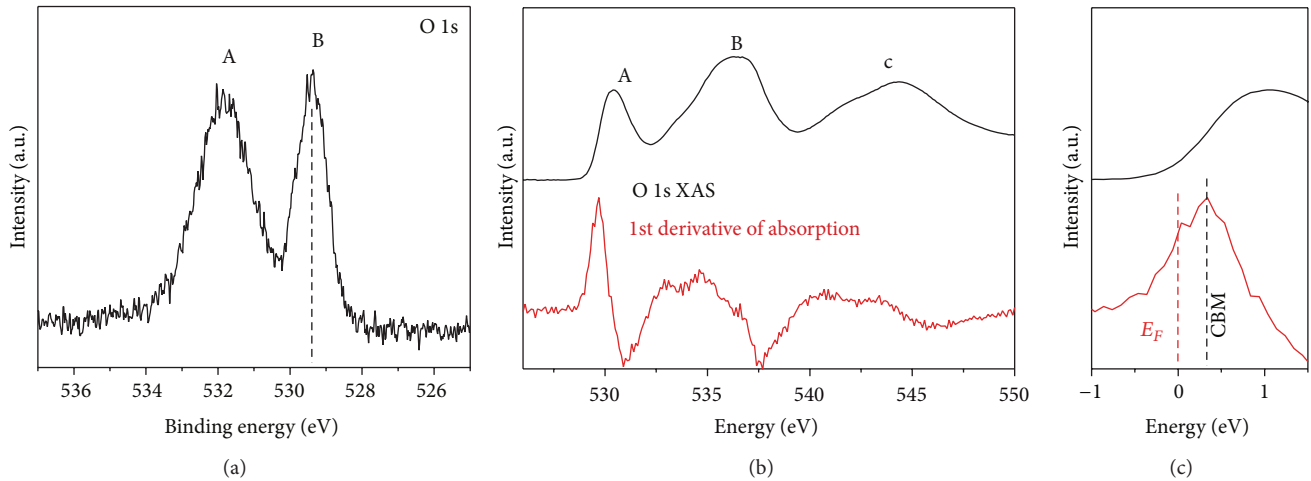


FIGURE 5: (a) O 1s core electron, (b) O 1s XAS and first derivative of absorption of LSMO thin film, and (c) expanded data (calibrated by O 1s binding energy) in the vicinity of the Fermi level.

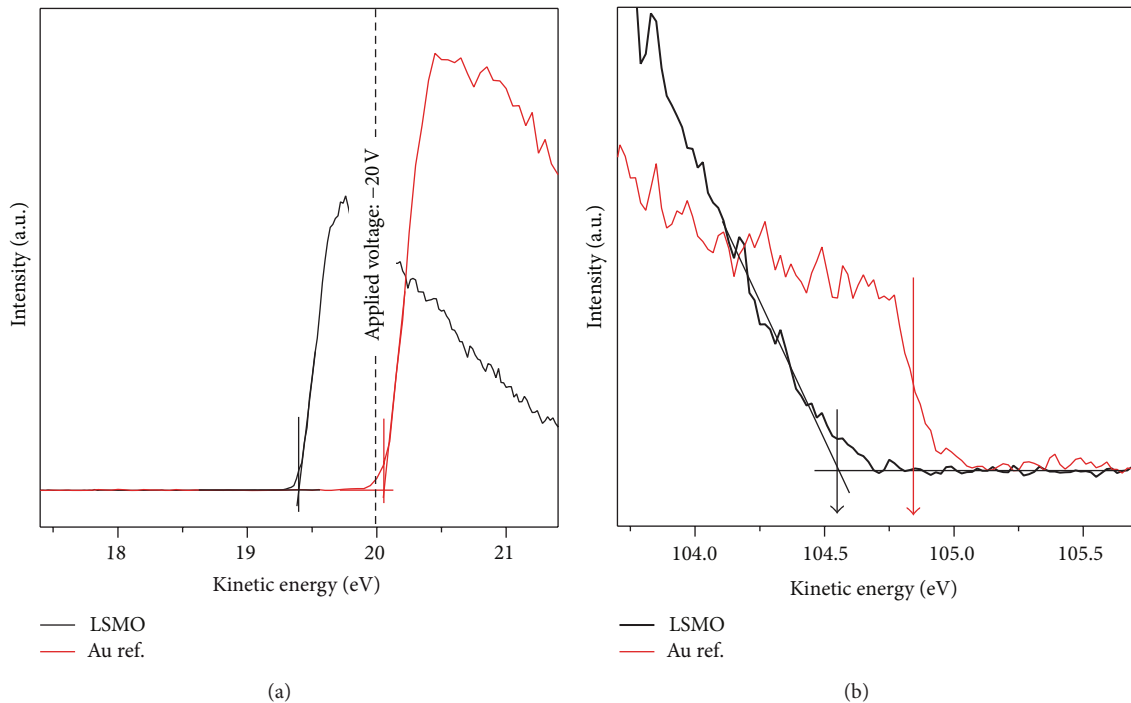


FIGURE 6: (a) Secondary cut-off and (b) valence band spectrum (in kinetic energy) of LSMO thin film and reference Au.

( $\text{La}_{0.4}\text{Gd}_{0.3}\text{Sr}_{0.3}\text{MnO}_3$ ) thin films to show changes in band structure of perovskite manganite according to A-site substitution. The measured values needed to complete the band structure are given in Table 1. As shown in Table 1, band gap widening with a decrease in electron affinity was observed according to A-site substitution. In perovskite manganites, the band structure is changed by A-site substitution, which induces structural distortion and/or change in band filling [15, 16]. In this case, the ratio of divalent and trivalent cations was fixed. Therefore, the change was induced from a structural distortion due to a smaller A-site cation, wherein the smaller A-site cation reduces Mn-O-Mn bond angle in

the Mn-O octahedral matrix. The decreased bond angle led to band narrowing and band gap widening. Therefore, a comparison study of band mapping, as shown in Table 1, showed a variation in the electronic structure of the material.

#### 4. Conclusions

In this study, we introduced a band structure analysis technique using soft X-ray spectroscopy with synchrotron radiation on a LSMO film. For band structure analysis, a variable energy source is required because unoccupied states should be measured. In the band structure analysis, proper

TABLE 1: Measured values for combining band structure of  $(\text{La}_{0.7}\text{Sr}_{0.3})\text{MnO}_3$ ,  $(\text{La}_{0.6}\text{Gd}_{0.1})\text{Sr}_{0.3}\text{MnO}_3$ , and  $(\text{La}_{0.4}\text{Gd}_{0.3})\text{Sr}_{0.3}\text{MnO}_3$  films.

	$E_F$ -VBM (①)	CBM- $E_F$ (④)	$E_G$ (⑤ = ① + ④)	$E_{WF}$ (⑥)	$E_{EA}$ (⑦)
$(\text{La}_{0.7}\text{Sr}_{0.3})\text{MnO}_3$	0.29 eV	0.34 eV	0.63 eV	4.80 eV	4.46 eV
$(\text{La}_{0.6}\text{Gd}_{0.1})\text{Sr}_{0.3}\text{MnO}_3$	0.39 eV	0.43 eV	0.82 eV	4.80 eV	4.37 eV
$(\text{La}_{0.4}\text{Gd}_{0.3})\text{Sr}_{0.3}\text{MnO}_3$	0.41 eV	0.54 eV	0.95 eV	4.80 eV	4.26 eV

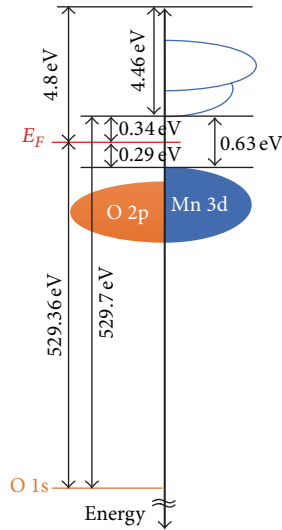


FIGURE 7: Complete band diagram of LSMO film.

energy calibration is critical because the variable energy source in the synchrotron does not guarantee an exact energy value, while a monochromatic energy source normally offers an exact energy value. Accurate band structure analysis is required to understand material properties, which could be achieved from a very accurate energy calibration using well-known materials like Au and  $\text{SiO}_2$ . In addition, a comparative study of various compositions can provide more meaningful data.

## Conflict of Interests

The authors declare that there is no conflict of interests regarding the publication of this paper.

## Acknowledgments

This work was supported by the Industrial Strategic Technology Development Program (10041926, Development of High-Density Plasma Technologies for Thin Film Deposition of Nanoscale Semiconductor and Flexible Display Processing) funded by the Ministry of Knowledge Economy (MKE, Korea). Experiments at PLS were supported in part by MSIP and POSTECH.

## References

- [1] J. Wang, J. B. Neaton, H. Zheng et al., "Epitaxial  $\text{BiFeO}_3$  multiferroic thin film heterostructures," *Science*, vol. 299, no. 5613, pp. 1719–1722, 2003.
- [2] W. Eerenstein, N. D. Mathur, and J. F. Scott, "Multiferroic and magnetoelectric materials," *Nature*, vol. 442, no. 7104, pp. 759–765, 2006.
- [3] R. von Helmolt, J. Wecker, B. Holzapfel, L. Schultz, and K. Samwer, "Giant negative magnetoresistance in perovskitelike  $\text{La}_{2/3}\text{Ba}_{1/3}\text{MnO}_x$  ferromagnetic films," *Physical Review Letters*, vol. 71, no. 14, pp. 2331–2333, 1993.
- [4] H. S. Lee, S. G. Choi, H.-H. Park, and M. J. Rozenberg, "A new route to the Mott-Hubbard metal-insulator transition: strong correlations effects in  $\text{Pr}_{0.7}\text{Ca}_{0.3}\text{MnO}_3$ ," *Scientific Reports*, vol. 3, article 1704, 2013.
- [5] Y.-J. Choi, S. C. Gong, C.-S. Park et al., "Improved performance of organic light-emitting diodes fabricated on Al-doped ZnO anodes incorporating a homogeneous Al-doped ZnO buffer layer grown by atomic layer deposition," *ACS Applied Materials & Interfaces*, vol. 5, no. 9, pp. 3650–3655, 2013.
- [6] Z. Zou, J. Ye, K. Sayama, and H. Arakawa, "Direct splitting of water under visible light irradiation with an oxide semiconductor photocatalyst," *Nature*, vol. 414, no. 6864, pp. 625–627, 2001.
- [7] D. A. Skoog and J. J. Leary, *Principles of Instrumental Analysis*, Saunders College Publishing, Orlando, Fla, USA, 6th edition, 1992.
- [8] R. Herrmann and C. Onkelinx, "Quantities and units in clinical chemistry: nebulizer and flame properties in flame emission and absorption spectrometry," *Pure and Applied Chemistry*, vol. 58, no. 12, pp. 1737–1742, 1986.
- [9] S. O. Kasap, *Principles of Electronic Materials and Devices*, McGraw-Hill, New York, NY, USA, 3rd edition, 2006.
- [10] Y. Tokura and Y. Tomioka, "Colossal magnetoresistive manganites," *Journal of Magnetism and Magnetic Materials*, vol. 200, no. 1, pp. 1–3–23, 1999.
- [11] M. Uehara, S. Mori, C. H. Chen, and S.-W. Cheong, "Percolative phase separation underlies colossal magnetoresistance in mixed-valent manganites," *Nature*, vol. 399, no. 6736, pp. 560–563, 1999.
- [12] P. G. Radaelli, M. Marezio, H. Y. Hwang, S.-W. Cheong, and B. Batlogg, "Charge localization by static and dynamic distortions of the  $\text{MnO}_6$  octahedra in perovskite manganites," *Physical Review B - Condensed Matter and Materials Physics*, vol. 54, article 8992, 1996.
- [13] V. M. Goldschmidt, "The laws of crystal chemistry," *Naturwissenschaften*, vol. 14, no. 21, pp. 477–485, 1926.
- [14] J. P. Zhou, J. T. McDevitt, J. S. Zhou et al., "Effect of tolerance factor and local distortion on magnetic properties of the perovskite manganites," *Applied Physics Letters*, vol. 75, no. 8, pp. 1146–1148, 1999.

- [15] M. B. Salamon and M. Jaime, "The physics of manganites: structure and transport," *Reviews of Modern Physics*, vol. 73, no. 3, pp. 583–628, 2001.
- [16] A. J. Millis, P. B. Littlewood, and B. I. Shraiman, "Double exchange alone does not explain the resistivity of  $\text{La}_{1-x}\text{Sr}_x\text{MnO}_3$ ," *Physical Review Letters*, vol. 74, no. 25, pp. 5144–5147, 1995.
- [17] K. Ebata, H. Wadati, M. Takizawa et al., "Chemical potential shift and spectral-weight transfer in  $\text{Pr}_{1-x}\text{Ca}_x\text{MnO}_3$  revealed by photoemission spectroscopy," *Physical Review B: Condensed Matter and Materials Physics*, vol. 74, no. 6, Article ID 064419, 2006.
- [18] T. Saitoh, A. E. Bocquet, T. Mizokawa et al., "Electronic structure of  $\text{La}_{1-x}\text{Sr}_x\text{MnO}_3$  studied by photoemission and x-ray-absorption spectroscopy," *Physical Review B*, vol. 51, Article ID 13942, 1995.
- [19] H.-S. Lee, C.-S. Park, and H.-H. Park, "Effect of  $\text{La}^{3+}$  substitution with  $\text{Gd}^{3+}$  on the resistive switching properties of  $\text{La}_{0.7}\text{Sr}_{0.3}\text{MnO}_3$  thin films," *Applied Physics Letters*, vol. 104, no. 19, Article ID 191604, 2014.
- [20] M. Abbate, F. M. F. de Groot, J. C. Fuggle et al., "Controlled-valence properties of  $\text{La}_{1-x}\text{Sr}_x\text{FeO}_3$  and  $\text{La}_{1-x}\text{Sr}_x\text{MnO}_3$  studied by soft-x-ray absorption spectroscopy," *Physical Review B*, vol. 46, no. 8, pp. 4511–4519, 1992.
- [21] H. Kurata and C. Colliex, "Electron-energy-loss core-edge structures in manganese oxides," *Physical Review B*, vol. 48, no. 4, pp. 2102–2108, 1993.
- [22] P. K. Ghosh, *Introduction to Photoelectron Spectroscopy*, John Wiley & Sons, New York, NY, USA, 1st edition, 1983.
- [23] J.-K. Yang and H.-H. Park, "Energy band structure and electrical properties of  $(\text{La}_2\text{O}_3)_{1-x}(\text{SiO}_2)_x$  ( $0 \leq x \leq 1$ )/ $n$ -GaAs (001) system," *Applied Physics Letters*, vol. 87, no. 20, Article ID 202102, pp. 1–3, 2005.
- [24] D.-J. Yun, K. Hong, S. H. Kim et al., "Multiwall carbon nanotube and poly(3,4-ethylenedioxythiophene): polystyrene sulfonate (PEDOT:PSS) composite films for transistor and inverter devices," *ACS Applied Materials and Interfaces*, vol. 3, no. 1, pp. 43–49, 2011.

